ARL-TR-8939 • Apr 2020

DEVCOM ARMY RESEARCH LABORATORY

A Comparison of Hybrid Reynolds-Averaged Navier–Stokes/Large-Eddy Simulation (RANS/LES) and Unsteady RANS Predictions of Separated and Transitional Flow for a Variable-Speed Power-Turbine Blade

by David T Booth

NOTICES

Disclaimers

The findings in this report are not to be construed as an official Department of the Army position unless so designated by other authorized documents.

Citation of manufacturer's or trade names does not constitute an official endorsement or approval of the use thereof.

Destroy this report when it is no longer needed. Do not return it to the originator.

ARL-TR-8939 ● APR 2020

A Comparison of Hybrid Reynolds-Averaged Navier–Stokes/Large-Eddy Simulation (RANS/LES) and Unsteady RANS Predictions of Separated and Transitional Flow for a Variable-Speed Power-Turbine Blade

David T Booth
Vehicle Technology Directorate, CCDC Army Research Laboratory

REPORT DOCUMENTATION PAGE

Form Approved
OMB No. 0704-0188

1. REPORT DATE *(DD-MM-YYYY)*	2. REPORT TYPE	3. DATES COVERED (From - To)
April 2020	Technical Report	5 September 2017–30 September 2018

4. TITLE AND SUBTITLE

A Comparison of Hybrid Reynolds-Averaged Navier–Stokes/Large-Eddy Simulation (RANS/LES) and Unsteady RANS Predictions of Separated and Transitional Flow for a Variable-Speed Power-Turbine Blade

5a. CONTRACT NUMBER

5b. GRANT NUMBER

5c. PROGRAM ELEMENT NUMBER

6. AUTHOR(S)

David T Booth

5d. PROJECT NUMBER

5e. TASK NUMBER

5f. WORK UNIT NUMBER

7. PERFORMING ORGANIZATION NAME(S) AND ADDRESS(ES)

CCDC Army Research Laboratory
ATTN: FCDD-RLV-A
Aberdeen Proving Ground, MD 21005

8. PERFORMING ORGANIZATION REPORT NUMBER

ARL-TR-8939

9. SPONSORING/MONITORING AGENCY NAME(S) AND ADDRESS(ES)

10. SPONSOR/MONITOR'S ACRONYM(S)

11. SPONSOR/MONITOR'S REPORT NUMBER(S)

12. DISTRIBUTION/AVAILABILITY STATEMENT

Approved for public release; distribution is unlimited.

13. SUPPLEMENTARY NOTES

14. ABSTRACT

A comparison of hybrid Reynolds-Averaged Navier–Stokes/Large-Eddy Simulation (RANS/LES) and unsteady RANS computations for unsteady separated flow prediction of a linear turbine-blade cascade operating with large incidence angle variation is described. The computations comprise a periodic single blade that represents the midspan section of a variable-speed power-turbine blade. A commercial off-the-shelf software package, Pointwise and CFD++, was used for the grid generation and computations. Simulations were assessed at incidence angles that represent turbine cruise and takeoff conditions. Comparisons of results for blade loading and loss were made to test data from NASA Glenn Research Center's Transonic Turbine Blade Cascade Facility. Comparisons of results for separation and transition predictions were made between the hybrid RANS/LES and RANS computations. Using the model that compared best to experimental results, the RANS Langtry–Menter model, further predictions of blade performance were made at engine-relevant pressure, temperature, and Mach conditions.

15. SUBJECT TERMS

power-turbine, computational fluid dynamics, CFD, Reynolds-Averaged Navier–Stokes/Large-Eddy Simulation, RANS/LES, turbine-blade cascade

16. SECURITY CLASSIFICATION OF:			17. LIMITATION OF ABSTRACT	18. NUMBER OF PAGES	19a. NAME OF RESPONSIBLE PERSON
a. REPORT	b. ABSTRACT	c. THIS PAGE			David T Booth
Unclassified	Unclassified	Unclassified	UU	51	19b. TELEPHONE NUMBER (Include area code) 410-278-9206

Contents

List of Figures

List of Tables

Acknowledgments

The author thanks AB Flegel and PW Giel for providing the experimental information and data used in this report.

1. Introduction

This study is part of an effort underway at the US Army Combat Capabilities Development Command Army Research Laboratory (ARL) to develop computational fluid dynamics (CFD) modeling and simulation capabilities for prediction of variable-speed power-turbine (VSPT) blade aerodynamic performance. Separation and transition flow physics occur with the VSPT turbine blade due to operation at low Reynolds numbers and a wide range of incidence angles. Improving prediction of separation and transition is an important area of research, as flow separation and transition have an impact on turbine blade performance and efficiency. The hybrid Reynolds-averaged Navier–Stokes/Large-Eddy Simulation (RANS/LES) approach is considered a promising technique to use in high Reynolds number–separated flow cases and has been used in a wide range of applications.[1] Evaluation and comparison of the hybrid RANS/LES and unsteady RANS capabilities of a commercial off-the-shelf (COTS) software were performed using a 3-D model of a candidate VSPT blade midspan section of a notional large civil tilt-rotor vehicle. The hybrid RANS/LES approach was chosen over LES to avoid the higher computational cost and to take advantage of the accuracy of RANS prediction of attached boundary layers and the strong prediction capability of LES in the separated flow regions.[2]

Power-turbine blades of conventional rotorcraft turboshaft engines are optimized to operate at nearly a fixed speed and a fixed incidence angle. The VSPT is a potential enabling technology for high-speed tilt-rotor aircraft where the power-turbine speed is decreased by as much as 51% during cruise flight compared with takeoff (hover) flight.[3] Significant design challenges exist for the VSPT due to this speed change, such as high work factors at cruise, large incidence angle variation (40°–60°), and low aft-stage Reynolds numbers at 28-kft cruise flight.[4] Incidence-tolerant turbine blade research was conducted by NASA Glenn Research Center (GRC) and ARL as a potential solution for maintaining turbine blade aerodynamic performance for variable-speed power-turbines.

Experiments were performed on a candidate VSPT blade midspan section in the Transonic Turbine Blade Cascade Facility at NASA GRC.[5,6] The experimental data of Flegel-McVetta et al.[5] and Flegel et al.[6] were acquired at low and high inlet-turbulence intensities, over a range of Reynolds numbers, at engine/mission-relevant exit Mach numbers, and over a wide range of incidence angles: +15.8° to –51.0°. The inlet flow of the experiment was well characterized in terms of inlet boundary-layer thickness, inlet turbulence intensity, and dissipation/length-scale using two-point hotwire measurements. Because the Reynolds numbers of the tunnel were higher than in the VSPT application, Flegel-McVetta et al.[5] chose to

test without an inlet turbulence grid so the flow would be transitional, mimicking low Reynolds operation at engine-relevant turbulence intensities. The experimental results indicated the design/cruise condition of the VSPT blade was highly loaded with transitional flow, while the takeoff condition represented an extreme off-design operating condition where the blade row was unloaded and the flow was very 2-D across the blade surface.[7]

Several simplifications exist with the turbine-blade cascade facility compared with a power-turbine in a gas turbine engine. The cascade facility has geometry simplifications of being a linear, nonrotating set of turbine blades where the blade cross section is constant in the spanwise direction and does not include a tip gap at the end. Differences in the operating environment include nonheated inlet air and absence of combustion gases. Simplifications that cause differences in the nature of the flow include the lack of a wake from stator blades and lack of rotational effects associated with Coriolis and centrifugal acceleration fields, the relative motion of the endwall, and impact of unsteadiness of downstream blade rows on the flow.[8] Therefore, the nature of transition mechanism in the turbine blade cascade is flow instability and separation-induced transition as opposed to bypass transition, which is the main transition mechanism in a gas turbine engine that occurs due to wakes from stators.[9] Nonetheless, the facility allows for highly 3-D flow and is useful for studying the aerodynamic effects of large incidence angle and Reynolds number changes, which are key challenges for VSPT applications.

CFD computations were performed at the turbine cruise condition corresponding to an inflow angle of 40° and takeoff condition corresponding to an inflow angle of –2.5°. These conditions were simulated at a low inlet turbulence intensity of 0.325% that will admit transitional flow on the blade surface, which is a significant challenge of the VSPT application.[4] In addition, computations were performed at the 40% design point Reynolds-number condition used by Flegel-McVetta et al.[5] to reduce the computational cost of the hybrid RANS/LES simulations. The computations were compared with measured blade loading and midspan loss provided by Flegel-McVetta et al.[5] Comparisons of separation and transition predictions of hybrid RANS/LES computations were made to time-accurate RANS computations of the VSPT cascade blade.

2. Experimental Description

The following summarizes the experimental test conducted in the Transonic Turbine Blade Cascade Facility at NASA GRC. Details of the experiment are given in Flegel-McVetta et al.[5,6]

2.1 Facility

The Transonic Turbine Blade Cascade Facility is a large-scale cascade that allows detailed flow field surveys and blade surface measurements.[10–12] The facility has a continuous run capability over a large relevant range of Reynolds and Mach numbers along with the ability to vary incidence over a 95° range. Details of the facility are shown in Fig. 1.

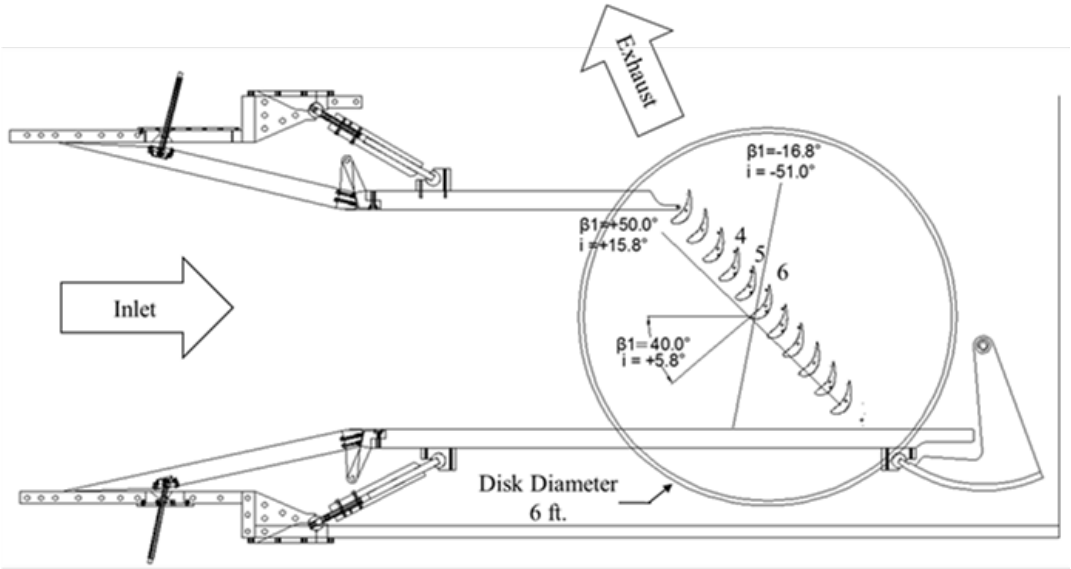

Fig. 1 Transonic Turbine Blade Cascade Facility

The cascade was made up of nominally 11 blades. The blade geometry is a scaled midspan section of a VSPT second-stage rotor.[13] Details of the blade geometry are shown in Fig. 2 and described in Table 1. Data were acquired for 10 incidence angles spanning $+15.8° \leq i \leq -51.0°$.[5,6] Two design incidence angles that correspond to takeoff ($i = -36.7°$) and cruise ($i = +5.8°$) were the focus of this CFD study. The design pressure ratio, *PR*, was 1.412, which corresponds to an exit isentropic Mach number of 0.72. A baseline flow condition was established by finding the lowest Reynolds number at which the tunnel could consistently maintain an exit Mach number of 0.72. The baseline Reynolds number, Re_b, was found to be 0.53×10^6.[14] Table 2 provides details of the test conditions that computations were compared with.

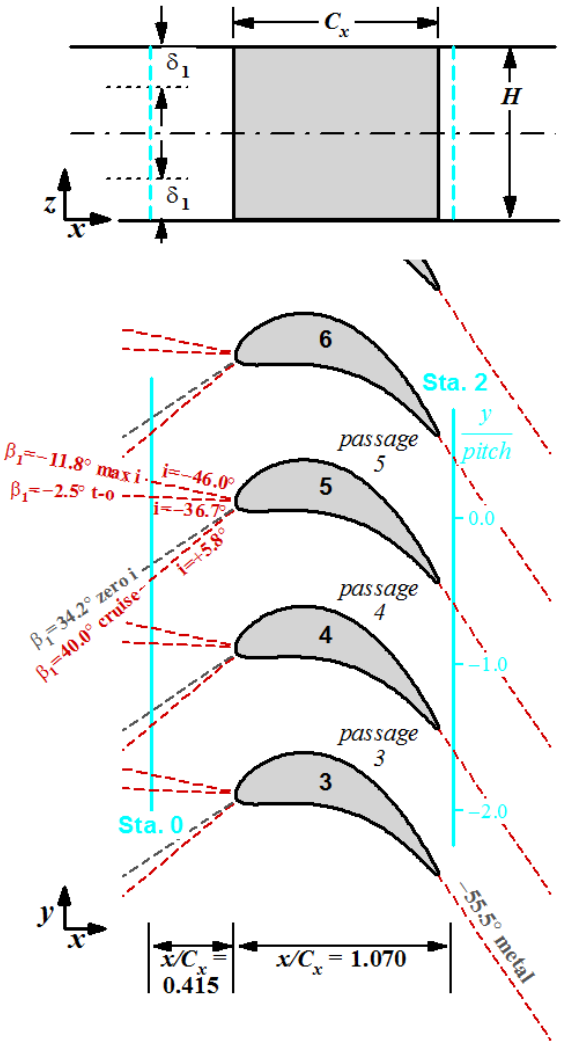

Fig. 2 VSPT blade details and measurement station locations

Table 1 VSPT blade description

Geometry	Value
Axial chord, C_x	180.57 mm (7.109 inches)
True chord	194.44 mm (7.655 inches)
Pitch, S	130.00 mm (5.119 inches)
Span, H	152.40 mm (6.000 inches)
Throat diameter	72.85 mm (2.868 inches)
Leading edge diameter	15.16 mm (0.597 inches)
Trailing edge diameter	3.30 mm (0.130 inches)
Stagger angle	20.35°
Inlet metal angle	34.2°
Uncovered turning	19.47°
Exit metal angle	−55.54°

Table 2 Angle and flow conditions used in the simulations

Incidence angle, i	Inlet angle, β_1	Inlet Re_{Cx}	Exit Re_{Cx}	Pressure ratio	Exit M_{is}	δ_{inlet} (inches)
−36.7° (take-off)	−2.5°	128,600	215,900	1.0886	0.350	1.69
+5.8° (cruise)	+40.0°	170,300	221,500	1.0891	0.351	1.63

2.2 Measurement Description

Total pressure data were acquired using a five-hole and three-hole pneumatic pressure probe installed 0.07 C_x downstream of the blade trailing edge.[14] This survey location is shown as Station 2 in Fig. 2 and traversed across three blade passages. For the i = −36.7° and i = +5.8° incidence angles, detailed half-span surveys were acquired over 26 spanwise and 62 pitchwise points. The overall estimated uncertainty in flow angle was ±1.5°, and the overall estimated uncertainty in total pressure coefficient was ±0.8%.[5]

The primary measurement blades, Blades 4, 5, and 6, were instrumented with pressure static taps located along 10%, 15%, 30%, and 50% span. Blade 5 was fully instrumented with 44 static taps on the pressure and suction side. To verify periodicity, Blade 4 had redundant taps located on the suction side of the blade, while Blade 6 had taps located on the pressure side. The blade static pressures were measured by an electronically scanned pressure system with ±15-psid modules referenced to atmosphere. A five-point calibration was performed automatically at least once per hour against a high-accuracy quartz pressure transducer. The absolute uncertainty of the pressure measurements was believed to be well within ±0.01 psi.[14] The inlet turbulence intensity, Tu, was characterized with a single-wire hotwire anemometer that was installed in the Station 0 survey plane.[11]

3. Computational Approach

This section contains the description of the computational approach used in the study. The first subsection highlights salient features of the flow solver, the second subsection describes the CFD mesh and mesh generation process, and the third subsection presents the computational parameters of the simulations.

3.1 Flow Solver

The 3-D time-resolved hybrid RANS/LES and RANS computations were performed on structured grids. Computations were run in parallel on a US Department of Defense Supercomputing Resource Center supercomputer. A COTS code was used with multiblock grids. For this study, CFD++ version 16.1.1 was the chosen COTS software.[15]

The selected equation set is a pressure-based compressible perfect gas Navier–Stokes solver. The spatial discretization used by the code is a multidimensional total variation diminishing polynomial interpolation determined through limited reconstructions over cells and/or nodes.[16] Spatial discretization is second-order with node-based polynomials. The local Courant number is used to accelerate convergence, and a second-order dual-time-stepping technique is selected for time-accurate computations.

A Batten–Goldberg hybrid RANS/LES model was used for the hybrid RANS/LES simulations. This model uses a modified form of the classical Smagorinsky model away from the walls and uses a two-equation nonlinear (cubic) k-epsilon turbulence model on RANS-type grids in attached boundary layers.[16] For the RANS simulations, the cubic k-epsilon model solves for the turbulence kinetic energy (k) and its dissipation rate (epsilon) and contains nonlinear terms that account for normal-stress anisotropy, swirl, and streamline curvature effects.[16] For the LES simulations, a subgrid scale (SGS) model in the code was implemented that removes the underlying numerical diffusion from the Smagorinsky eddy viscosity SGS model, which results in the model behaving less diffusive in free shear layers[17] The Batten–Goldberg hybrid RANS/LES model is resistant to ambiguous grid densities and permits the activation of RANS and LES in different flow regions, providing a balanced numerical approach to complex turbulent flows.[1,18,19]

Time-accurate RANS computations were performed for comparison with the hybrid RANS/LES results. A turbulence model comparison study was performed comparing computational results with experimental data and is described in Section 4.1. The Langtry–Menter model compared best to experimental data and was used for comparison with hybrid RANS/LES model results. Details of this model are described in Section 4.1.

3.2 CFD Mesh

For hybrid RANS/LES grid sensitivity analysis, three grids of different cell density and domain type were used. The grids were generated from the experimental blade coordinate data using Pointwise version 17.3[20] and are depicted in Fig. 3. The

computational domain of the grids included a single blade with periodic boundary conditions in the pitchwise directions as a representation of a periodic linear cascade. This representation was chosen to simplify the model and reduce the amount of computational resources needed for the simulation, and it was assumed that this simplification would not have a great effect on accuracy compared with a full cascade passage model. The inlet boundary condition was located at approximately 0.415 C_x upstream of the blade leading edge to correspond to the location of experimental inlet measurement Station 0. The exit boundary condition was located approximately 1.0 C_x downstream of the trailing edge to correctly capture the wake region. A uniform back-pressure imposition boundary condition was placed there to match the measured exit pressure. The grid was rotated about the center of the blade in the z-direction to change the incidence of the blade with respect to the incoming flow, which was fixed in the x-direction. A boundary layer grid thickness for the blade was estimated based on the maximum thickness at the blade trailing edge, which was estimated using a one-seventh power-law equation for turbulent flow on a flat plate.[21]

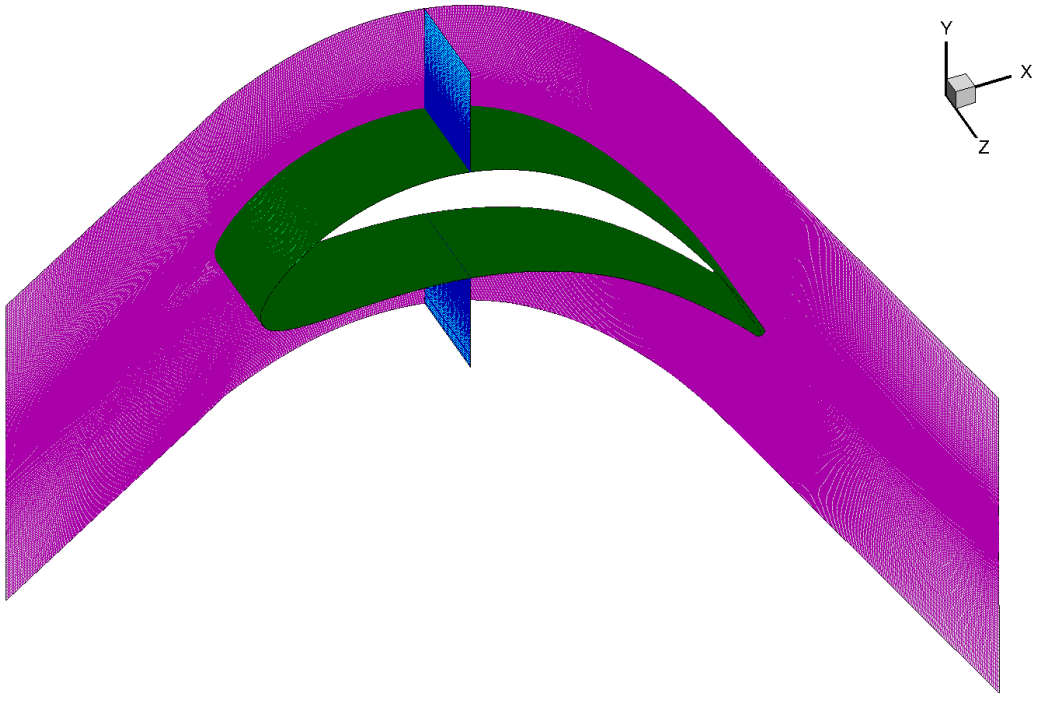

Fig. 3 3-D grid of VSPT blade

An 8-million-cell 3-D structured mesh was used for initial hybrid RANS/LES and RANS computation comparisons. For this grid, the boundaries included the endwall and modeled half the span of the midspan geometry due to symmetry in the spanwise direction. Modeling half the span was done to reduce the size of the mesh

and thus reduce computational cost. It was assumed that this simplification would not have a significant effect on the accuracy of the hybrid RANS/LES computations. There was no blade tip gap, and a viscous no-slip wall boundary condition was used for the endwall boundary. A Musker inlet velocity profile boundary condition was used for the inlet boundary. This boundary condition provided by the CFD++ code for internal flow parallel to one or more solid walls allows the user to prescribe a fully developed turbulent boundary-layer profile for all mean-flow and turbulence-related quantities.[16] The generated boundary-layer profile is based on Musker's 1979 formulation in conjunction with a compressibility transformation and temperature fit due to Van Driest.[16] Turbulence quantities in the boundary layer were determined as functions of the mean-velocity derivatives, based on an assumption of local equilibrium.[16]

A boundary-layer grid was used to accurately resolve the viscous boundary layer of the endwall and was determined using an estimated maximum thickness based on the experimental data. An initial distance from the wall to the first wall-adjacent centroid, Δy_{init}, of 5.0×10^{-6} m was chosen with a tanh boundary layer spacing and a 1.1 expansion factor to obtain 73 points in the boundary layer normal to the wall. A boundary-layer grid was created for the blade with a Δy_{init} of 7.6×10^{-7} m and 69 points in the boundary layer normal to the blade surface for a y+ value less than 0.5.

Dimensions of the grid were 480 × 167 × 78 nodes in streamwise, pitchwise, and spanwise directions, respectively. There were 784 cells around the airfoil with the entire grid containing 8 million cells. Previous grid sensitivity analysis of this grid was performed using RANS computations that showed solution results were independent of grid refinement at 4 million cells, so it was expected that the 8-million cell grid would perform adequately for the RANS computations presented in this report.[14]

A 32-million-cell hybrid RANS/LES mesh was created similar to the 8-million-cell grid except the mesh excluded the endwall with only the middle section of the blade outside of the experimentally measured boundary layer of the endwalls modeled. This section represented 20% of the actual span. A symmetry boundary condition was used for the spanwise direction. This grid was constructed so that RANS computations would be performed in the attached boundary-layer region of the turbine blade where the higher-aspect ratio cells were located. In the blade boundary-layer region, the grid was constructed with a Δy_{init} of 1.3×10^{-6} m for a y+ value less than 0.5. A 1.1 expansion factor was used until reaching the region outside the boundary layer where more-uniform grid cells were employed for the LES computations. A total of 54 points was used in the boundary layer normal to the blade surface.

Cells in the LES region of the grid were constructed to be as isotropic as possible. Cell length in the LES region was determined based on the formulation recommended by Spalart et al. of $\delta/10$, where δ represents the boundary-layer thickness on the blade.[1] Based on an estimated maximum laminar boundary-layer thickness, cell length was chosen to be 2.7×10^{-4} m.

Dimensions of the grid were 996 × 224 × 130 nodes in the streamwise, pitchwise, and spanwise directions, respectively. There were 1172 cells around the airfoil, with the entire grid containing 32 million cells. Determination of overall grid fineness was based on recommendations for similar grids used for LES computations for low-pressure turbine blades summarized in a survey performed by Ameri in 2016.[22]

A third hybrid RANS/LES mesh was created with 82 million cells that included the same boundaries with endwall details as the initial 8-million-cell grid. For the endwall boundary layer, a Δy_{init} of 7.0×10^{-6} m was chosen with a tanh boundary-layer spacing and a 1.1 expansion factor to obtain 250 points in the boundary layer normal to the wall. A boundary layer grid was created for the blade with a Δy_{init} of 7.6×10^{-7} m and 45 points in the boundary layer normal to the blade surface.

Cells in the LES region of the grid were constructed with an overall cell length of 5×10^{-4} m. Dimensions of the grid were 976 × 274 × 329 nodes in streamwise, pitchwise, and spanwise directions, respectively. There were 1228 cells around the airfoil, with the entire grid containing 82 million cells.

3.3 Computational Parameters

Computations were performed at the cruise and takeoff conditions listed of +40° and –2.5°, respectively. The turbulence length scale used for the computations was based on length scale measurements made for the Energy Efficient Engine cascade turbine blade tested at similar *Tu* and M in the GRC Transonic Turbine Blade Cascade Facility.[23]

Due to the unsteady nature of the flow through the VSPT cascade at the takeoff condition at low inlet turbulence levels, as determined by Booth et al.,[14] time-accurate computations were performed for all computations. For temporal resolution, a time step of 2×10^{-6} s was used based on the ratio of mesh spacing in the unsteady wake region to maximum relevant wave speed. Implicit dual time-stepping with 10 subiterations was used. Time-stepping was chosen based on estimations of time of flight through the blade passage so that there were approximately 1000 time steps for one flow-through. After convergence of the

solution was obtained, the solutions were time averaged over approximately 20 flow-through times to have sufficient data for statistical analysis.

For solution convergence, computations were carried out until sufficient reduction was obtained for the transient residuals from the inner (subiteration) steps of the dual time-stepping simulations. The residuals are the full right-hand side (RHS) for the quasi steady-state inner problem, as shown in the following equation:

$$\frac{\partial(\vec{q}V)}{\partial t} + \frac{\partial(\vec{q}V)}{\partial \tau} + \vec{F}_{inv} + \vec{F}_{visc} + \vec{S} \cdot V = 0 \tag{1}$$

or

$$\frac{\partial(\vec{q}V)}{\partial \tau} = -\left(\frac{\partial(\vec{q}V)}{\partial t} + \vec{F}_{inv} + \vec{F}_{visc} + \vec{S} \cdot V\right), \tag{2}$$

$$RHS$$

where $\vec{q}$ is the dependent variable vector, V is the cell volume, τ is the pseudo time, $\vec{F}_{inv}$ is the inviscid flux, $\vec{F}_{visc}$ is the viscous flux, and $\vec{S}$ is the source term.[16] At each pseudo time step, for each equation in each cell, the absolute value of the RHS was computed and the residuals were the average of this quantity over all cells for each equation.[16] The solutions were considered to have converged when the inner residuals had reduced by at least 0.05.

4. Results and Discussion

The main objective of the study was to investigate and compare the computational accuracy of the hybrid RANS/LES and time-accurate RANS methods in predicting the unsteady separated and transitional flow of the VSPT blade. The results were compared with experimental measurements for blade loading and the wake region for the cruise and takeoff angles. Comparison of flow separation and transition predictions were made between hybrid RANS/LES and RANS methods using velocity iso-surface plots and skin friction plots.

4.1 RANS Turbulence Model Selection

A RANS turbulence model comparison study was performed comparing computational results with experimental data using the k-epsilon, Langtry–Menter, cubic k-epsilon, k-omega, and Shear Stress Transport (SST) models. Details of these models can be found in Metacomp Technologies Inc.[16] and Wilcox.[24] Comparison results of the cruise condition operating at 40% of design $Re_{Cx,2}$ showed the Langtry–Menter, SST, and k-epsilon models performed best for blade loading at 50% span (Fig. 4). Overall, very good agreement is observed for these

models; however, neither model performed best in predicting the wake, as they all overpredicted it and located it higher in the pitchwise location (Fig 5.). Prior comparisons of these models were also performed by Metacomp Technologies, Inc., using an Aerospatiale A airfoil and S809 airfoil example. The Langtry–Menter model and the k-epsilon in conjunction with an algebraic transition model had the best agreement with the data for these examples.[16] Based on these studies, the Langtry–Menter model was chosen for further comparisons. The Langtry–Menter transition prediction model is a four-equation turbulence closure that solves transport equations for k, turbulence inverse time-scale (ω), intermittency, and transition momentum thickness Reynolds number.[16]

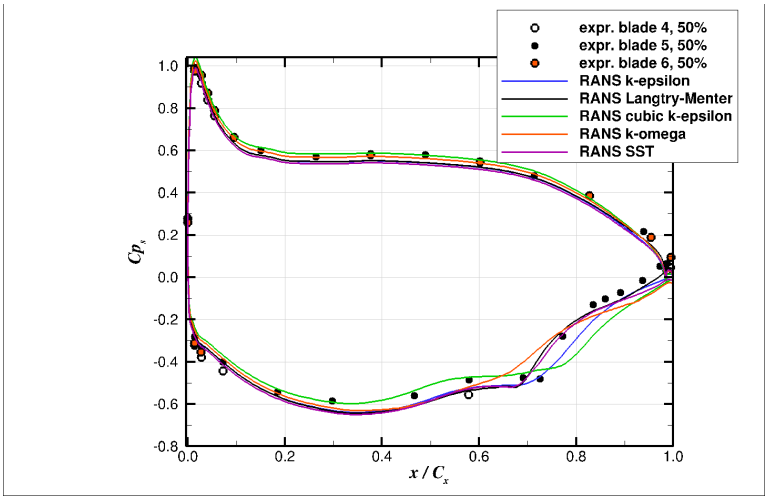

Fig. 4 Comparison of RANS model computations to experiment for 40% design $Re_{Cx,2}$ cruise-condition pressure distributions at 50% span

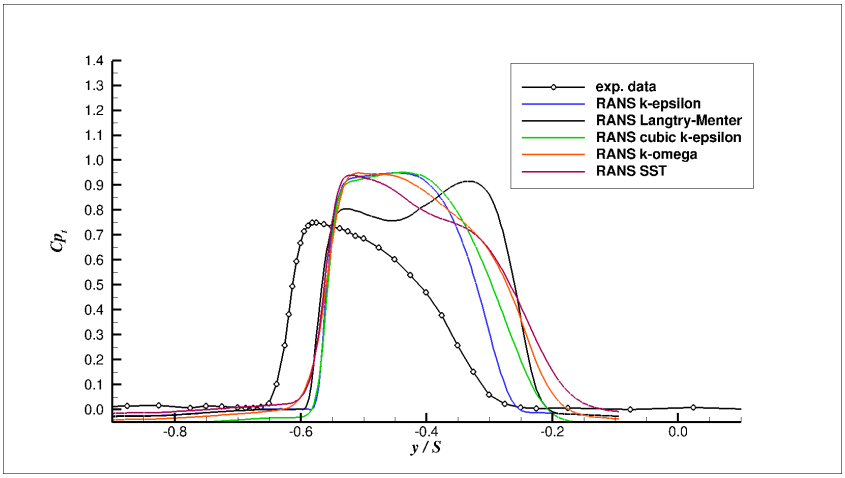

Fig. 5 Comparison of RANS computations to experiment for 40% design $Re_{Cx,2}$ cruise-condition total pressure loss at 0.07 axial chord downstream of midspan location

4.2 RANS Reynolds Number Comparisons

A Reynolds number comparison study was performed at low *Tu* conditions using the Langtry–Menter model. RANS simulations were run at the 40%, 100%, and 400% design $Re_{Cx,2}$ cruise conditions and the results were compared with measurements. As can be seen in Figs. 6a and 6b, results for the 40% and 100% design $Re_{Cx,2}$ conditions were in excellent agreement with measurements for pressure distributions at all spanwise locations. As seen in Fig. 6c, results for the 400% design $Re_{Cx,2}$ condition at all spanwise locations tended to overpredict pressure-side pressure distributions and leading-edge suction-side pressure distributions, while they slightly underpredicted trailing-edge suction-side pressure distributions.

As shown in Fig. 7, results for all Reynolds numbers tended to slightly overpredict the pitchwise location of the wake compared with measurements. In addition, results for the 40% and 100% design $Re_{Cx,2}$ conditions overpredicted the magnitude of total pressure loss from the wake. The 400% design $Re_{Cx,2}$ results matched closest to measurement for magnitude of total pressure loss; however, the simulation overestimated the inlet P_t resulting in an incorrectly low offset of overall values of Cp_t.

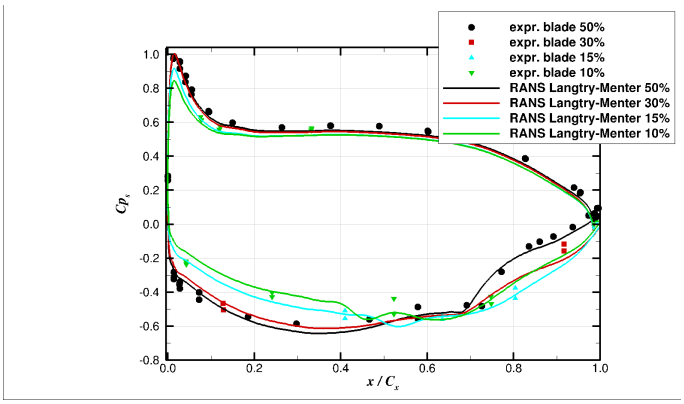

(a)

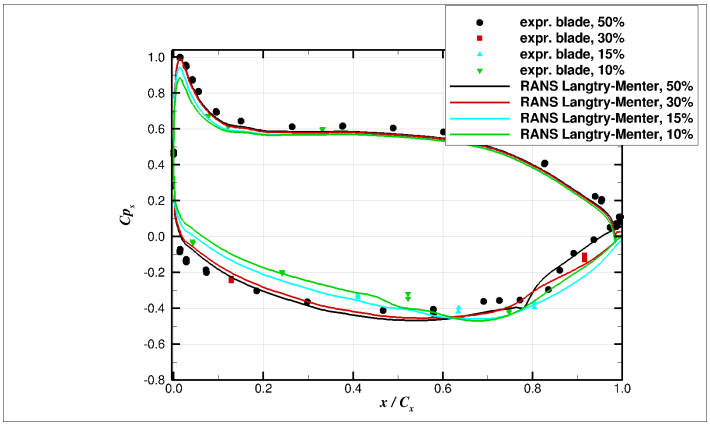

(b)

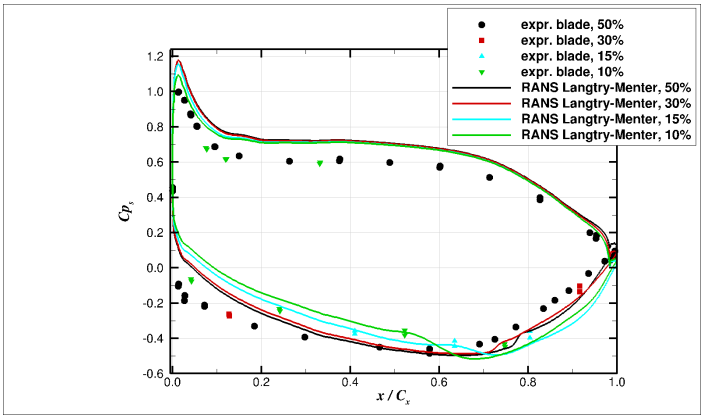

(c)

Fig. 6 Reynolds number comparisons of RANS computations to experiment for cruise-condition pressure distributions: a) 40% design $Re_{Cx,2}$, b) 100% design $Re_{Cx,2}$, and c) 400% design $Re_{Cx,2}$

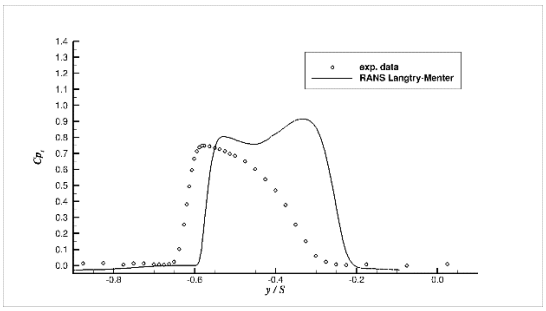

(a)

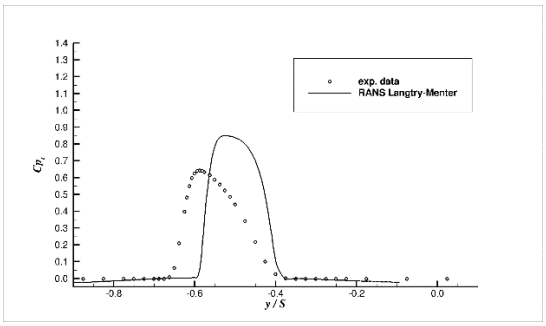

(b)

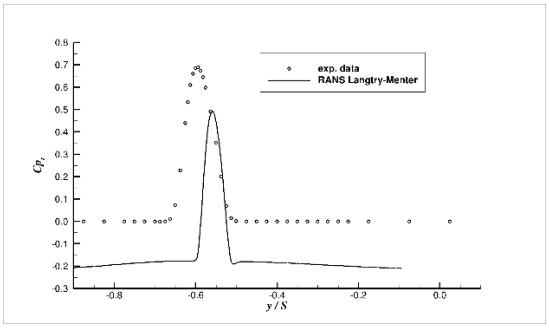

(c)

Fig. 7 Reynolds number comparisons of RANS computations to experiment for cruise-condition total pressure loss at 0.07 axial chord downstream of midspan location: a) 40% design $Re_{Cx,2}$, b) 100% design $Re_{Cx,2}$, and c) 400% design $Re_{Cx,2}$

4.3 RANS Turbulence Intensity Comparisons

A turbulence intensity comparison was performed for the cruise and takeoff conditions at 100% design $Re_{Cx,2}$ using the Langtry–Menter model, and the results were compared with measurements for blade loadings and losses. As shown in Figs. 8 and 9b, results for the high *Tu* are in good agreement with measurements,

except they slightly underpredict blade loadings on the pressure side. Comparisons of Fig. 8 with Fig. 6b for the cruise-condition pressure distributions show that simulation results for high *Tu* do not predict the midspan suction-side separation/reattachment at x/C_x = 0.75 that is suggested by the low *Tu* results. Similarly, comparisons of Figs. 9a and 9b for the takeoff-condition pressure distributions show that results for high *Tu* do not predict the suction- and pressure-side separations and reattachments at x/C_x = 0.85 and x/C_x = 0.05, respectively, suggested by the low *Tu* results. This is consistent with expectations that the higher *Tu* energizes flow, making it more resistant to separation.

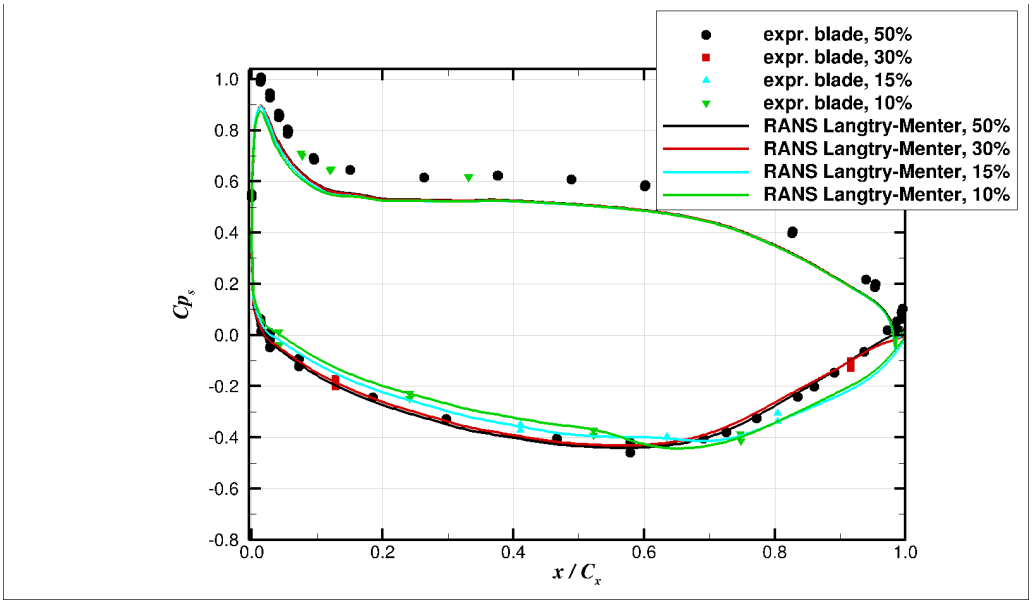

Fig. 8 Comparison of RANS computation with experiment for cruise-condition pressure distributions at *Tu* level of 7.4%

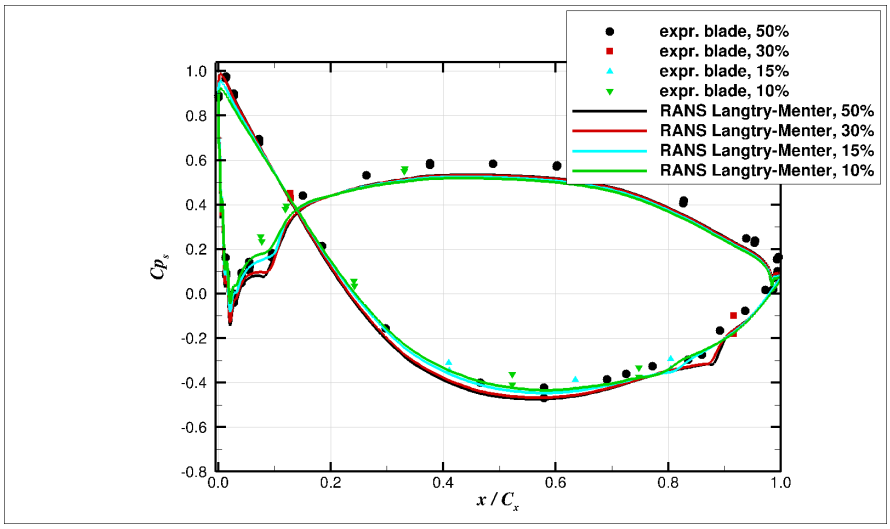

(a)

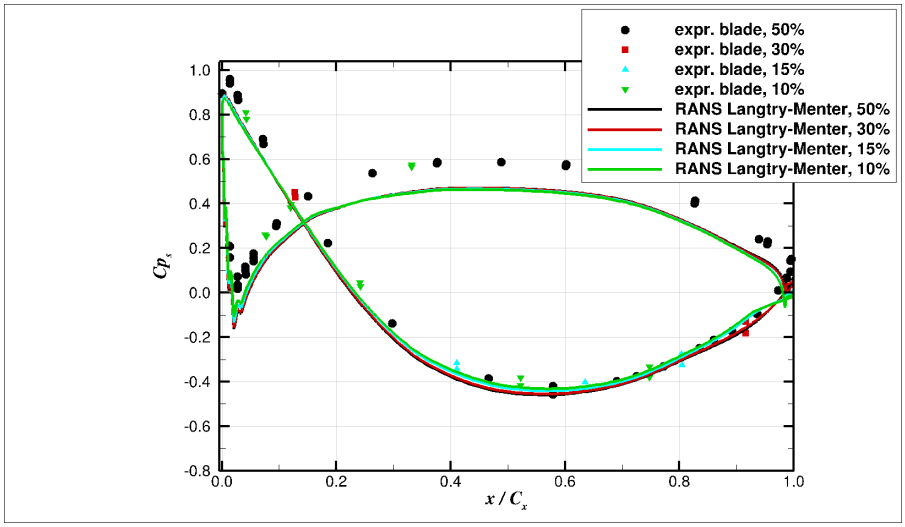

(b)

Fig. 9 Turbulence Intensity comparisons of RANS computations with experiment for takeoff-condition pressure distributions: a) *Tu* level of 0.325%, b) *Tu* level of 7.4%

For cruise-condition total pressure loss from the wake, the high *Tu* results (Fig. 10) appear to compare better with the narrower measured wake; however, the results are offset due to the simulation underestimating the inlet P_t, resulting in incorrectly high overall values of Cp_t. For the takeoff-condition total pressure loss from the wake, the low *Tu* results (Fig. 11a) appear to match the measurements slightly better than the high *Tu* results (Fig. 11b). Again, the high *Tu* results have incorrectly high offset overall values of Cp_t. All wake results overpredict the location of the wake in the pitchwise direction.

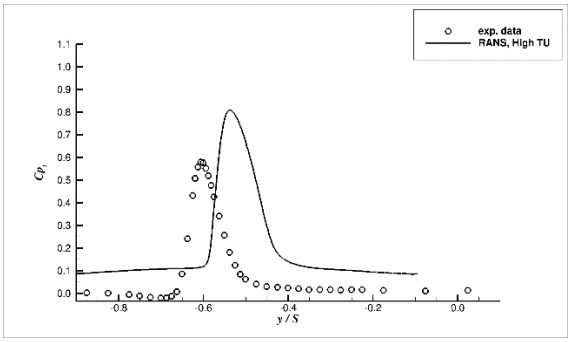

Fig. 10 Comparison of RANS computations with experiment for cruise-condition total pressure loss at 0.07 axial chord downstream of midspan location for *Tu* level of 7.4%

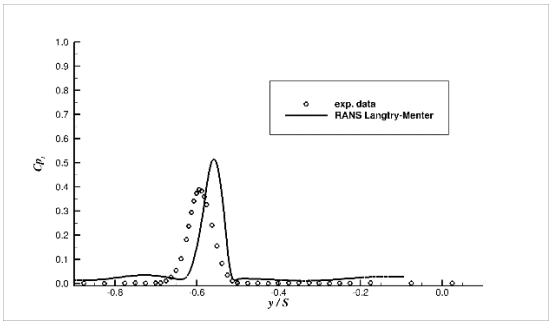

(a)

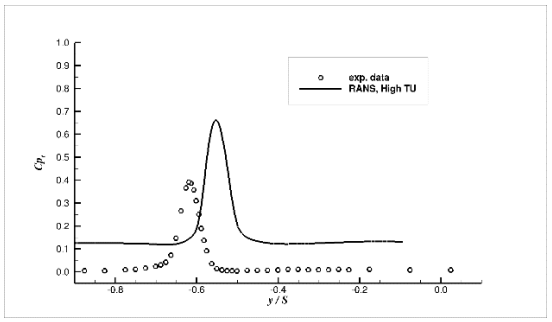

(b)

Fig. 11 Turbulence intensity comparisons of RANS computations with experiment for takeoff-condition total pressure loss at 0.07 axial chord downstream of midspan location: a) *Tu* level of 0.325% and b) *Tu* level of 7.4%

4.4 Hybrid RANS/LES Grid Sensitivity Analysis

A study was performed to observe sensitivity of accuracy of results to changes in grid fineness in the resolution of fluid flow scales in the chordwise and pitchwise directions. Comparison plots for the time-averaged midspan pressure distributions for the cruise condition are shown in Fig. 12, which shows that results compare best with measurements for the grid with 82 million cells. The 8- and 32-million-cell

grids show significant differences in results compared with the experiment for the suction-side trailing edge. Comparison plots for time-averaged downstream total pressure loss for the cruise condition are shown in Fig. 13, which shows that results compare best with measurements for the 82-million-cell grid. Based on this study, it was decided to use the 82-million-cell grid, and all further results presented in this report were obtained using this grid.

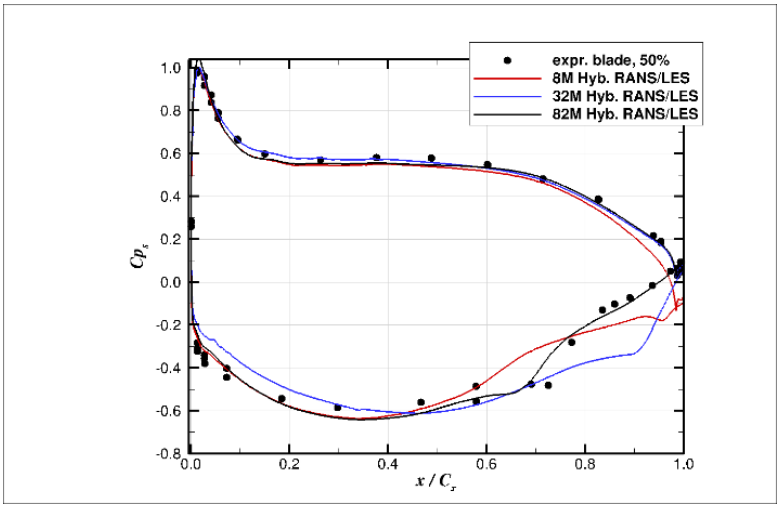

Fig. 12 Comparison of grid resolution to experiment for cruise-condition midspan pressure distribution predictions

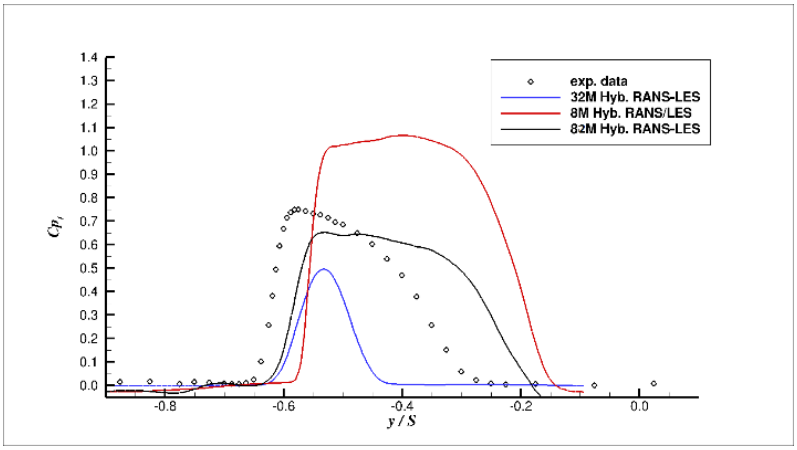

Fig. 13 Comparison of grid resolution with experiment for cruise-condition total pressure loss at 0.07 axial chord downstream of trailing edge at midspan

4.5 Comparison of RANS and Hybrid RANS/LES Results

4.5.1 Pressure Distributions

Comparisons of hybrid RANS/LES and time-accurate RANS computational results with the experimental measurements of the cruise-condition blade pressure

distributions were made. As shown in Figs. 14 and 15, spanwise plots of results for the hybrid RANS/LES model show overall good agreement with RANS Langtry–Menter results and measurements, except close to the endwall where RANS Langtry–Menter results match closer to experiment. All results predict a midspan suction side separation/reattachment at x/C_x = 0.65–0.75 suggested by experiment.

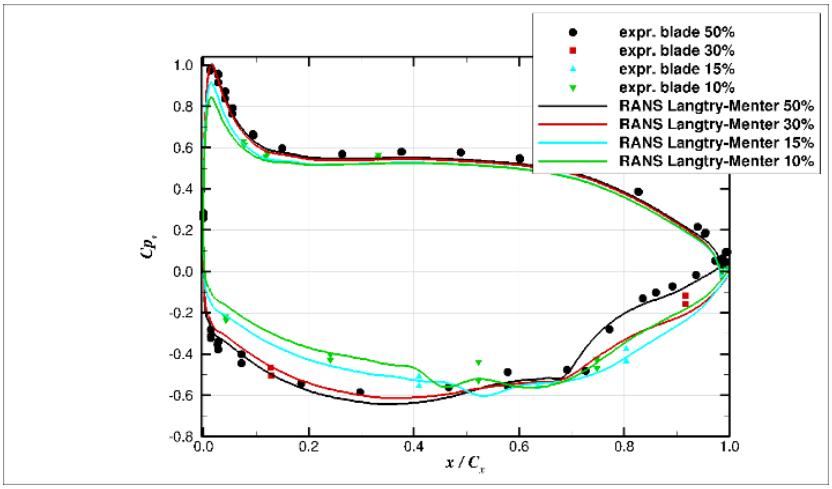

Fig. 14 Spanwise comparison of RANS computations to experiment for cruise-condition pressure distribution

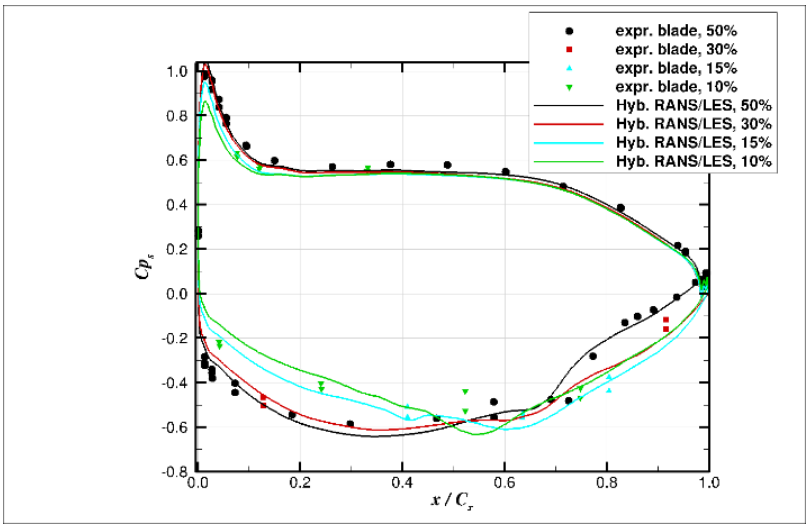

Fig. 15 Spanwise comparison of hybrid RANS/LES computations with experiment for cruise-condition pressure distributions

Comparisons of hybrid RANS/LES and time-accurate RANS computational results to measurements for the takeoff-condition midspan blade pressure distributions were made. In addition, computations using the RANS realizable k-epsilon turbulence model were compared. The highly negative incidence (–36.7°) produces

an inverted pressure distribution in the leading edge region of the blade, with the loading reverting to nominal beyond 20% of the chord from the leading edge.[12] Comparisons of spanwise plots of the RANS and hybrid RANS/LES results (Fig. 16) show that on the suction side, the RANS Langtry–Menter model compares closest to the measurements. The RANS Langtry–Menter model correctly predicts a plateau on the suction side at midspan and 30% span, suggesting possible separation at x/C_x = 0.75–0.85; however, the hybrid RANS/LES results do not. On the pressure side the RANS Langtry–Menter and hybrid RANS/LES results compare closest to the measurements in predicting the plateau in the experimental data, suggesting possible separation at x/C_x = 0.05–0.15.

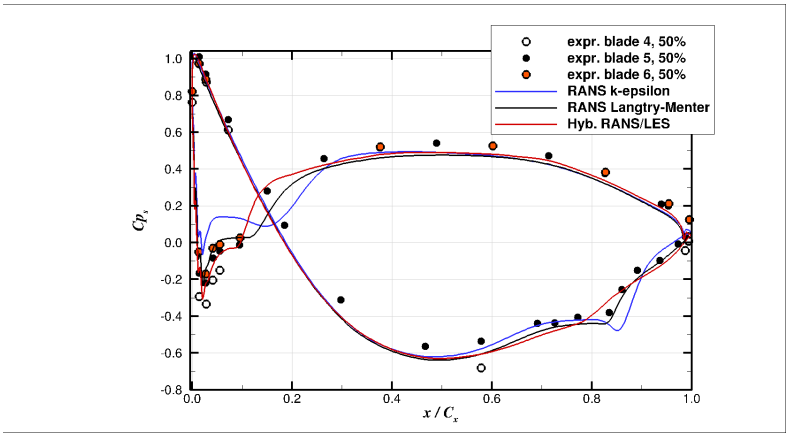

Fig. 16 Spanwise comparison of RANS and hybrid RANS/LES computations with experiment for takeoff-condition midspan pressure distributions

4.5.2 Exit Total Pressure

Comparisons of computational results to experimental measurements for the cruise-condition wake region were made. Figure 17 compares plots of computed and measured midspan total pressure loss at 7% C_x downstream of the blade. The RANS models both overpredicted the maximum Cp_t value, while the hybrid RANS/LES results slightly underpredicted it. All results slightly overpredicted the pitchwise location of the wake. The hybrid RANS/LES results compared best with measurements in terms of shape, size, and height of the wake. Comparisons of computational results to experimental measurements for the takeoff-condition wake region were made. Figure 18 compares plots of computed and measured midspan total pressure loss at 7% C_x downstream of the blade. All results overpredicted the maximum Cp_t value, with the hybrid RANS/LES results matching closest to measurements. All results slightly overpredicted the pitchwise location of the wake. The hybrid RANS/LES results compared slightly better than the RANS Langtry–Menter results in terms of shape and size of the wake.

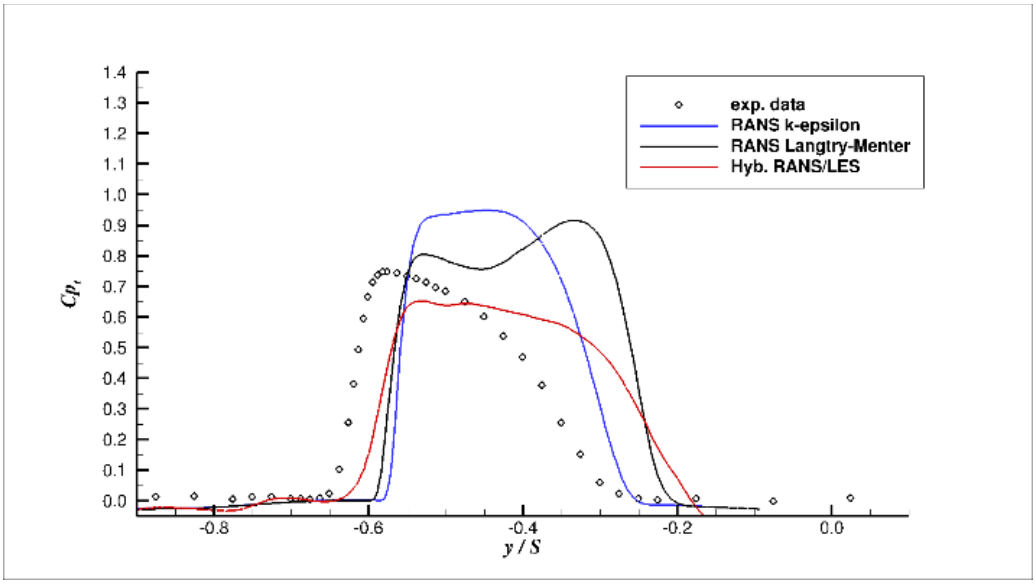

Fig. 17 Comparison of hybrid RANS/LES and RANS computations with experiment for cruise-condition total pressure loss at 0.07 axial chord downstream of trailing edge at midspan

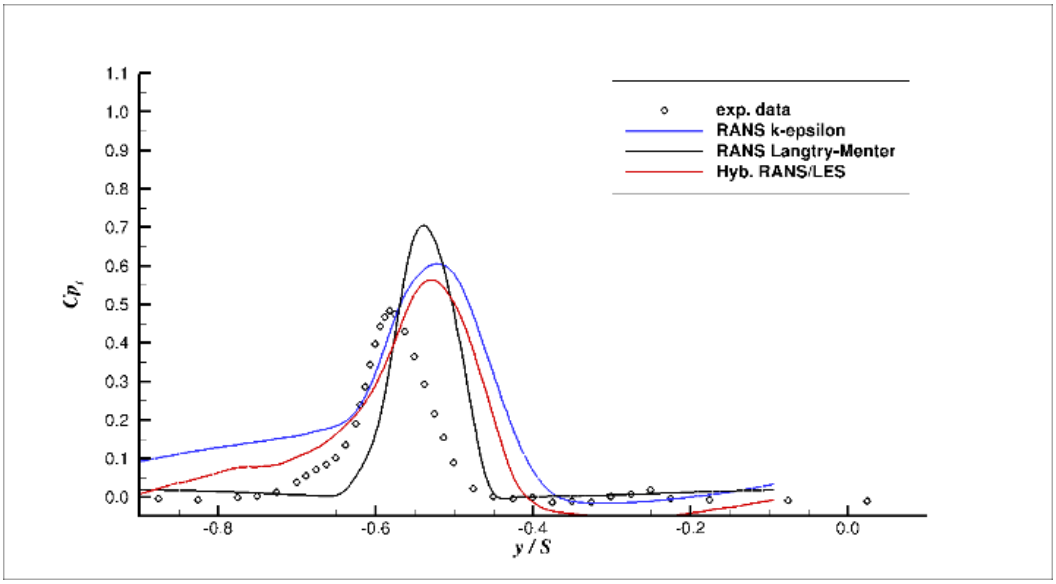

Fig. 18 Comparison of hybrid RANS/LES and RANS computations with experiment for takeoff-condition total pressure loss at 0.07 axial chord downstream of trailing edge at midspan

4.5.3 Flow Visualization

Velocity iso-surface plots of flow in the negative *x* direction were created for the cruise condition to guide in identifying regions of separation on the blade. As seen in Fig. 19 for the RANS Langtry–Menter results, there are two regions of shallow separation predicted on the suction side centered at midspan. A separation bubble

is located at approximately x/C_x = 0.65–0.75, and separation starts again at x/C_x = 0.80, continuing to the trailing edge. Separation is also present on the blade along the endwall starting at x/C_x = 0.75 and continuing to the trailing edge. In Fig. 20 the plot for the hybrid RANS/LES results shows a similar separation at midspan on the suction side at approximately x/C_x = 0.65–0.75. Another separation is predicted near the trailing edge, centered at approximately z/H = 0.25. No separation appeared on the pressure side for either model.

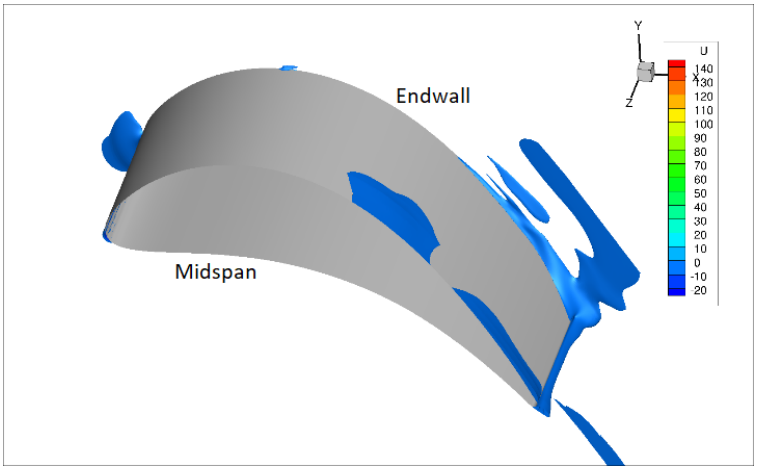

Fig. 19 RANS Langtry–Menter: velocity iso-surfaces of suction-side separation for cruise condition (meters per second)

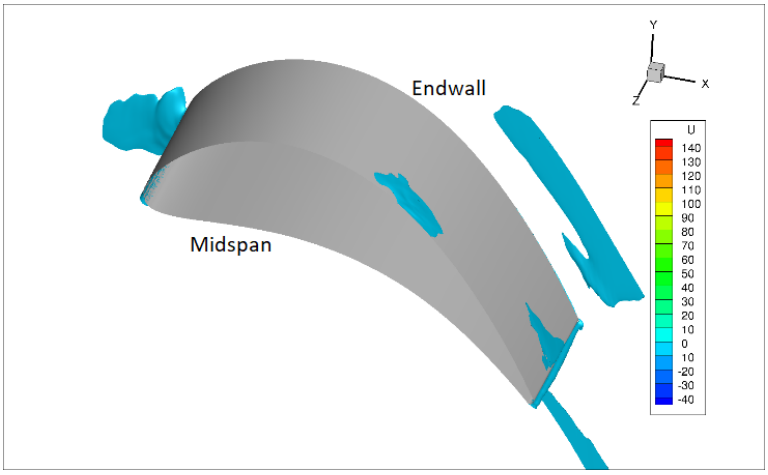

Fig. 20 Hybrid RANS/LES: velocity iso-surfaces of suction-side separation for cruise condition (meters per second)

As shown in Fig. 21, the RANS Langtry–Menter results for the takeoff condition predict a region of shallow separation on the suction side located at approximately x/C_x = 0.70–0.85 and spanning from approximately z/H = 0.20–0.50. Another zone of separation is also present on the blade near the trailing edge centered at

approximately z/H = 25%. On the pressure side (Fig. 22), a wide, shallow band of separation is predicted spanning across the blade close to the leading edge. In Fig. 23 the plot for the hybrid RANS/LES results shows a similar but narrower separation on the pressure side spanning across the blade close to the leading edge. No separation appeared on the suction side for the hybrid RANS/LES model.

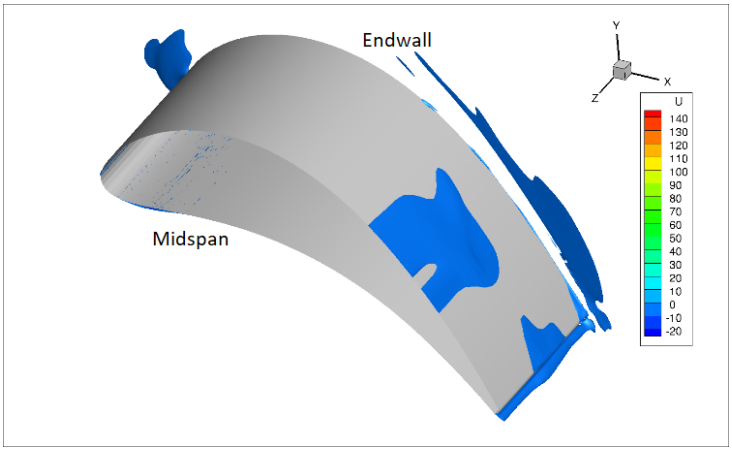

Fig. 21 RANS Langtry–Menter: velocity iso-surfaces of suction-side separation for takeoff condition (meters per second)

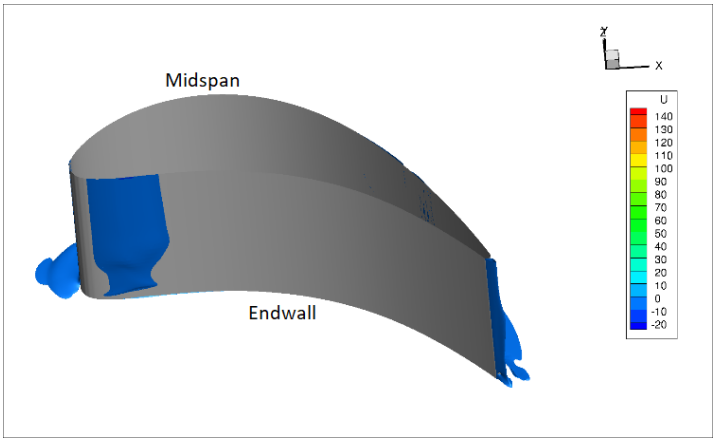

Fig. 22 RANS Langtry–Menter: velocity iso-surfaces of pressure-side separation for takeoff condition (meters per second)

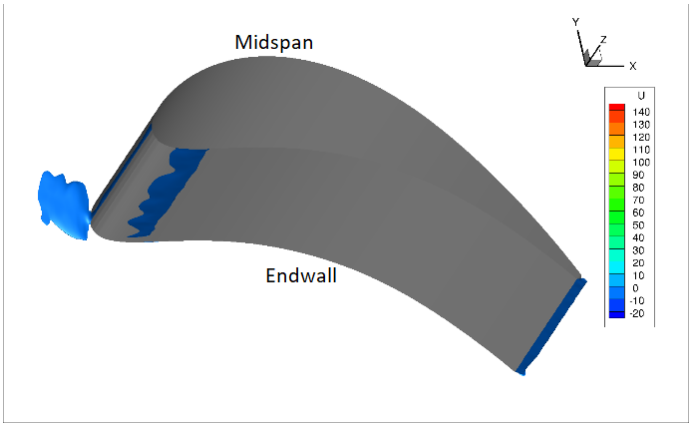

Fig. 23 Hybrid RANS/LES: velocity iso-surfaces of pressure-side separation for takeoff condition (meters per second)

4.5.4 Skin Friction Analysis

As shown in Fig. 24, the RANS Langtry–Menter results for the cruise condition predict laminar flow on the suction side at midspan leading to a likely separation-induced transition to turbulent flow around $x/C_x = 0.70$. In the spanwise direction, transition is very 3-D, occurring successively earlier approaching the endwall. For the pressure side (Fig. 25), transition appears to occur close to the leading edge and is fairly consistent in the spanwise direction.

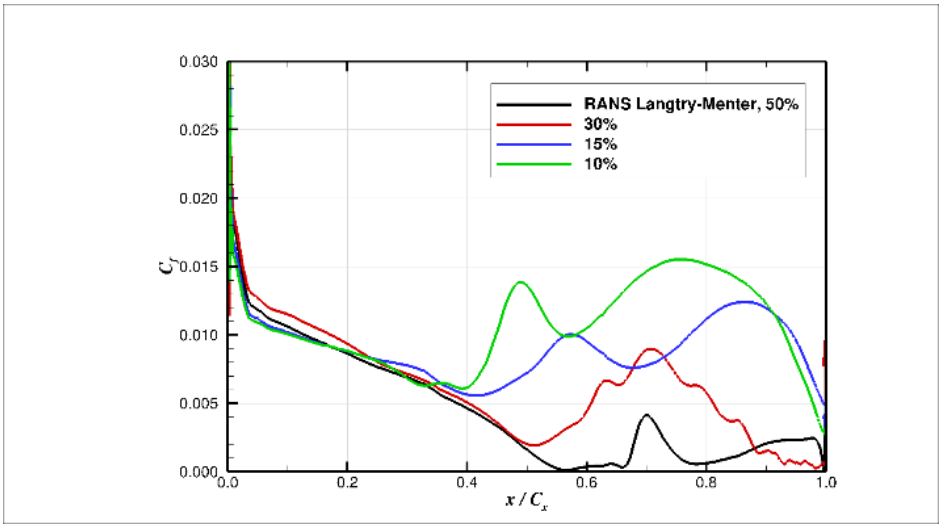

Fig. 24 Skin friction plots for RANS Langtry–Menter cruise-condition suction side at four spanwise locations

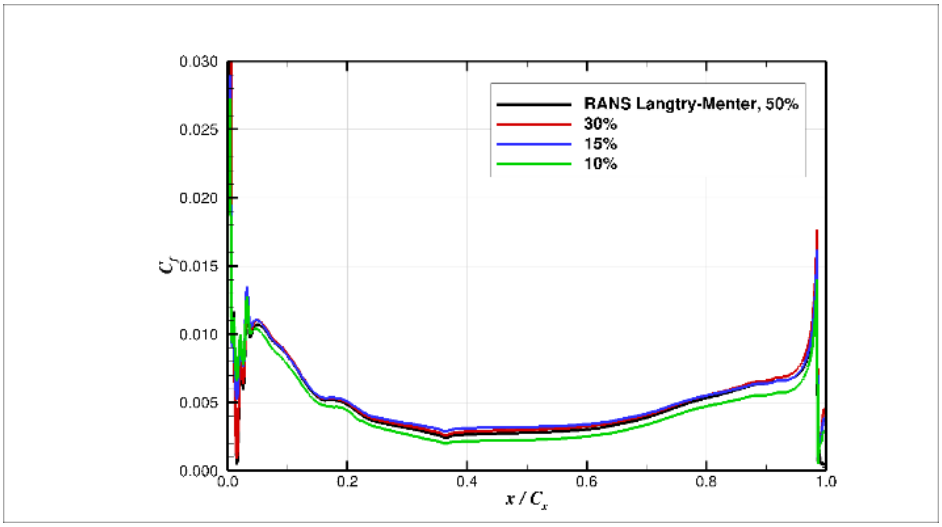

Fig. 25 Skin friction plots for RANS Langtry–Menter cruise-condition pressure side at four spanwise locations

The hybrid RANS/LES results for the suction side (Fig. 26) show a similar trend as the RANS Langtry–Menter results and predict transition at midspan at $x/C_x = 0.75$. In the spanwise direction, transition is also very 3-D but occurs earlier than the RANS Langtry–Menter results closer to the endwall. For the pressure side (Fig. 27), transitions appear similar to the RANS Langtry–Menter results occurring close to the leading edge.

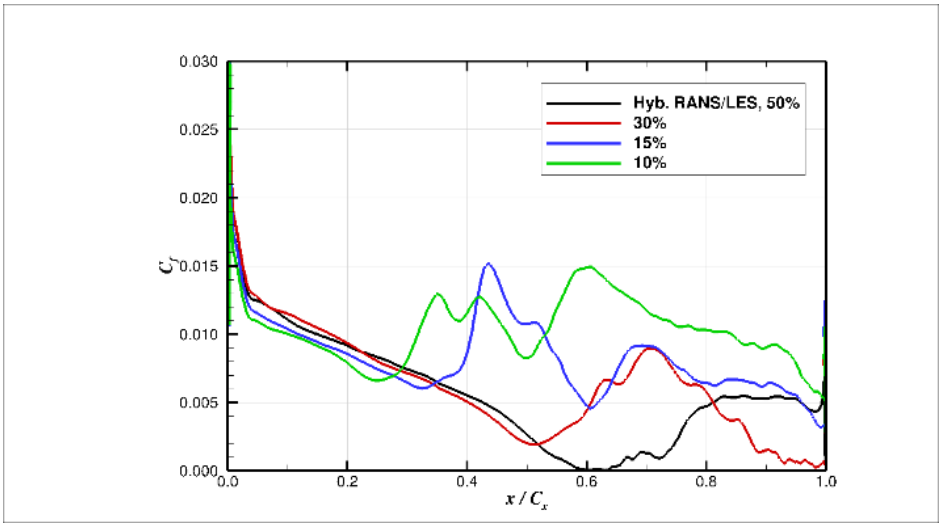

Fig. 26 Skin friction plots for hybrid RANS/LES cruise-condition suction side at four spanwise locations

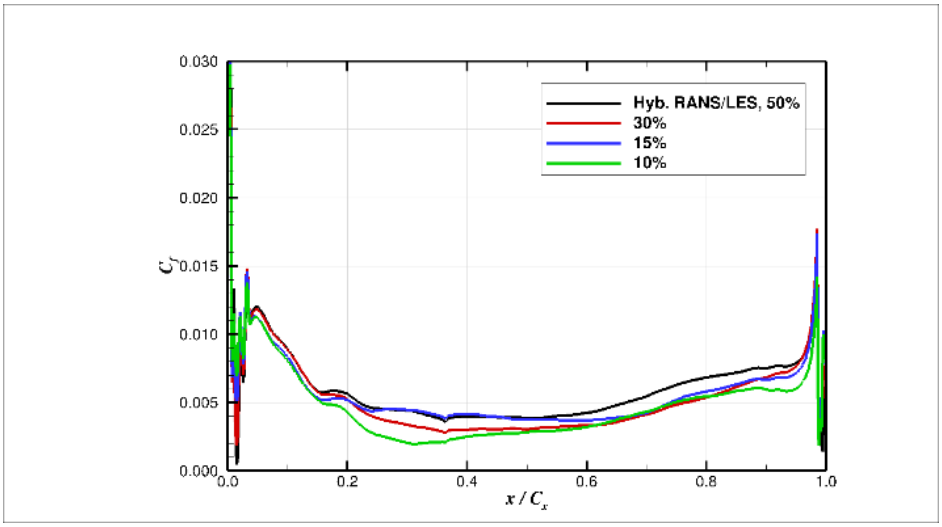

Fig. 27 Skin friction plots for hybrid RANS/LES cruise-condition pressure side at four spanwise locations

As shown in Fig. 28, the RANS Langtry–Menter results for the takeoff condition predict laminar flow on the suction side at midspan leading to a probable separation-induced transition to turbulent flow at approximately $x/C_x = 0.80$. In the spanwise direction, transition occurs slightly sooner closer to the endwall, and there is reduced three-dimensionality for transition location compared with the cruise condition, which is consistent with expectations, as the blade is lightly loaded at the takeoff condition. For the pressure side (Fig. 29), transition appears to occur at approximately $x/C_x = 0.10$ at midspan, and there is small spanwise variation in transition location observed in the results.

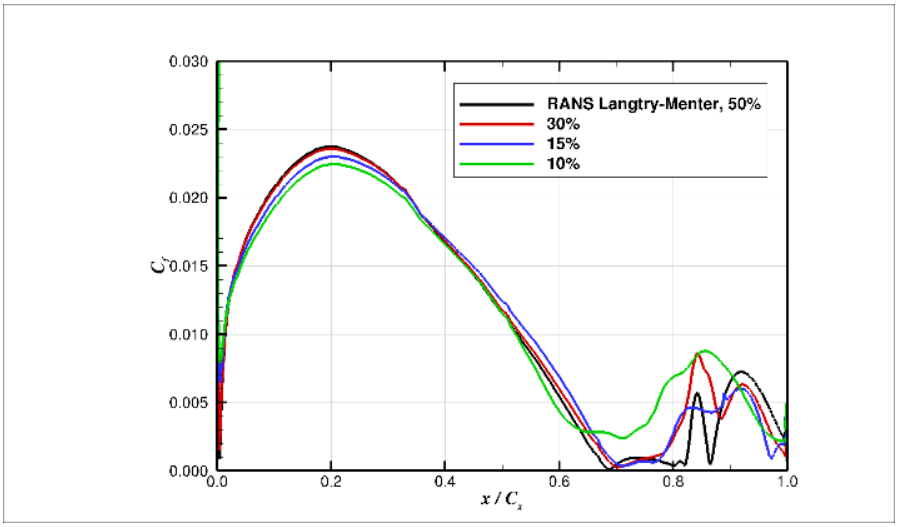

Fig. 28 Skin friction plots for RANS Langtry–Menter takeoff-condition suction side at four spanwise locations

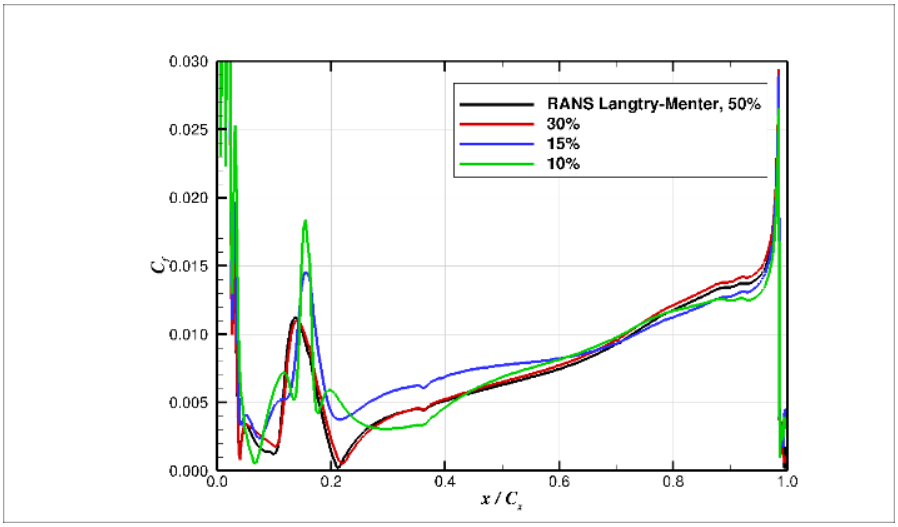

Fig. 29 Skin friction plots for RANS Langtry–Menter takeoff-condition pressure side at four spanwise locations

The hybrid RANS/LES results for the suction side (Fig. 30) show a similar trend as the RANS Langtry–Menter results, predicting transition at midspan at approximately $x/C_x = 0.80$. In the spanwise direction, transition locations are very similar to RANS Langtry–Menter results. For the pressure side (Fig. 31), transition locations are very similar to the RANS Langtry–Menter results.

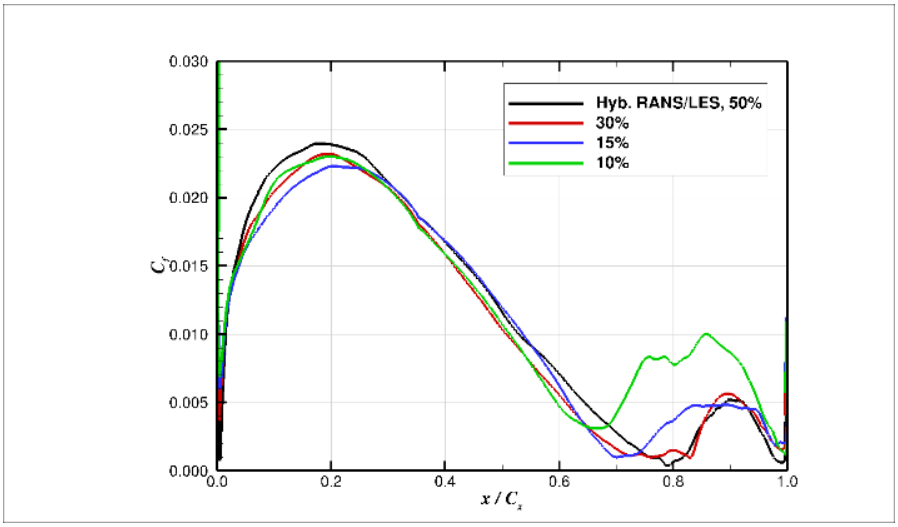

Fig. 30 Skin friction plots for hybrid RANS/LES takeoff-condition suction side at four spanwise locations

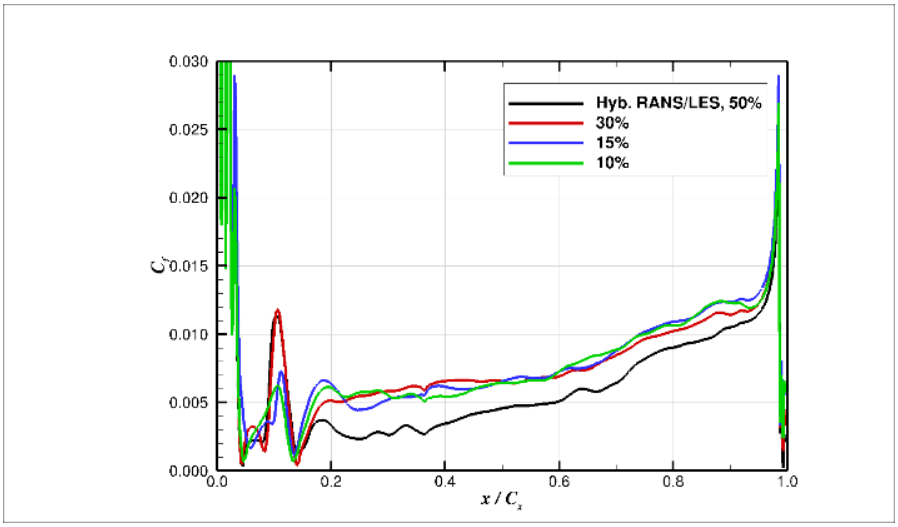

Fig. 31 Skin friction plots for hybrid RANS/LES takeoff-condition pressure side at four spanwise locations

4.6 Prediction of Performance at Engine-Relevant Conditions

Simulations of the VSPT cascade blade were performed at engine-relevant pressures, temperatures, and Mach numbers taken from proposed operating conditions for the VSPT listed in Suchezky and Cruzen.[25] These values represented a proposed low Reynolds-number cruise condition and a high Reynolds-number sea-level takeoff condition. The RANS Langtry–Menter model was chosen to perform these performance predictions because overall this model compared better with the GRC VSPT blade-cascade-facility measurements than the hybrid RANS/LES model and is less computationally expensive. As no data were collected at these engine-relevant conditions, there were no measurements to compare with these predictions.

4.6.1 Flow Visualization

The cruise condition velocity iso-surface plot (Fig. 32) of flow in the negative x direction reveals a large region of separation at midspan that starts at approximately $x/C_x = 0.65$ and continues to the trailing edge. A large endwall separation is also occurring that traverses across the blade toward midspan at the trailing edge. No separation appeared on the pressure side.

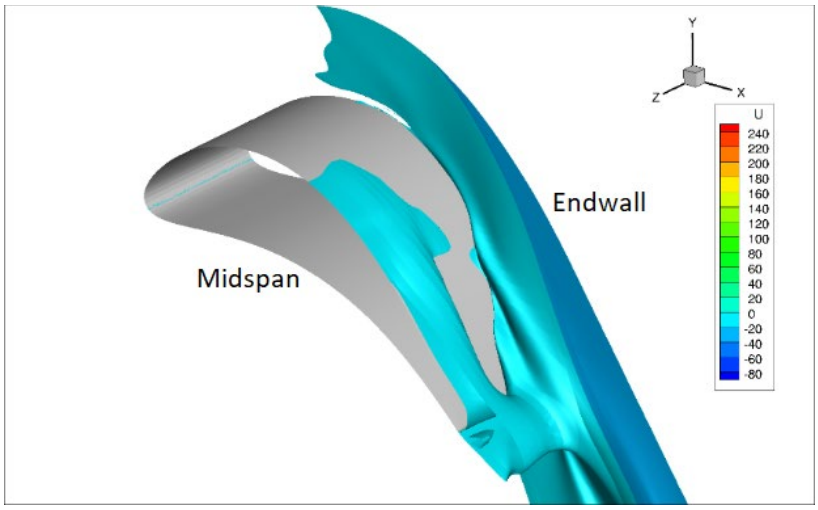

Fig. 32 RANS Langtry–Menter: velocity iso-surfaces of suction-side separation for cruise- condition at engine-relevant conditions (meters per second)

Takeoff-condition velocity iso-surface plots of flow in the negative x direction (Figs. 33 and 34), show similar trends of separation and location as the RANS Langtry–Menter simulations run at the ambient temperature conditions for suction and pressure sides.

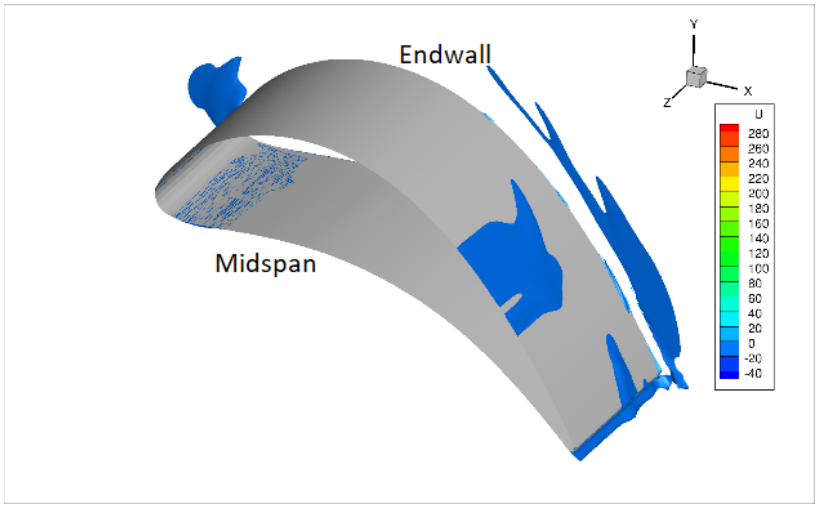

Fig. 33 RANS Langtry–Menter: velocity iso-surfaces of suction-side separation for takeoff condition at engine-relevant conditions (meters per second)

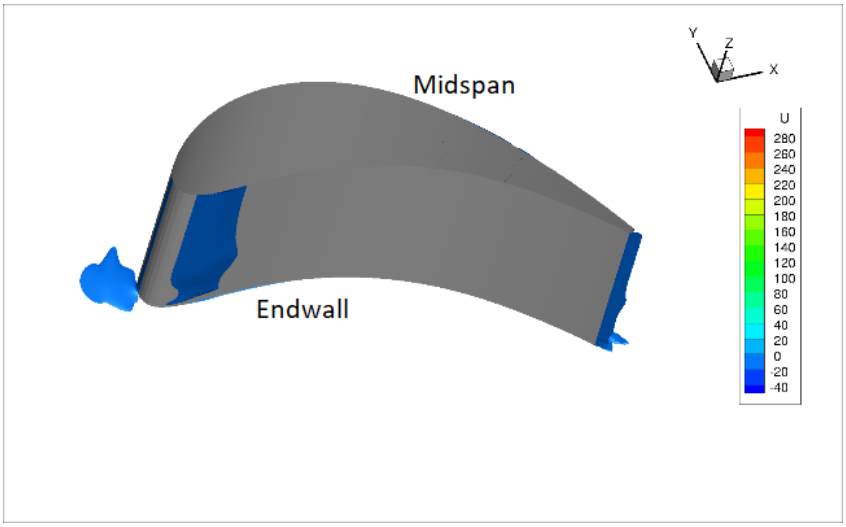

Fig. 34 RANS Langtry–Menter: velocity iso-surfaces of pressure-side separation for takeoff condition at engine-relevant conditions (meters per second)

4.6.2 Skin Friction Analysis

As shown in Figs. 35 and 36, skin friction plots for the cruise and takeoff conditions, respectively, show a similar trend as the RANS Langtry–Menter simulations run at the ambient temperature conditions for both suction and pressure side; however, the overall values of C_f are lower.

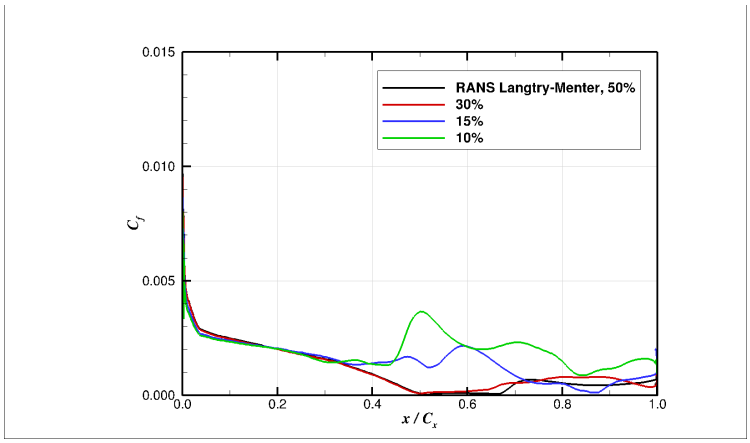

(a)

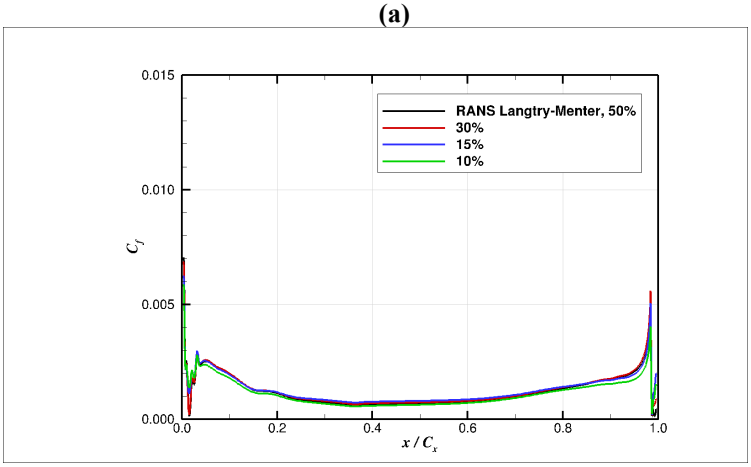

(b)

Fig. 35. Skin friction plots for RANS Langtry–Menter cruise condition at engine-relevant conditions at four spanwise locations: a) suction side and b) pressure side

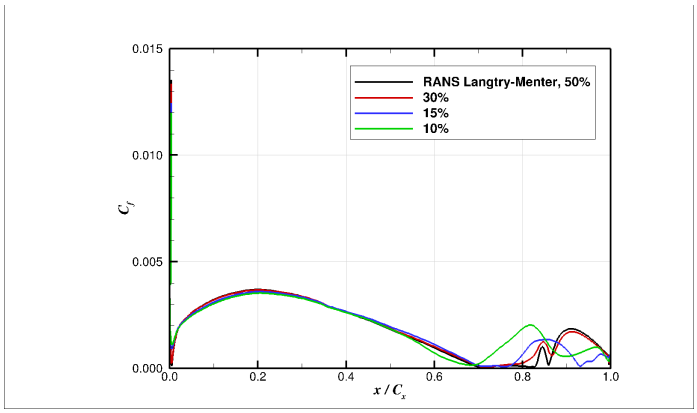

(a)

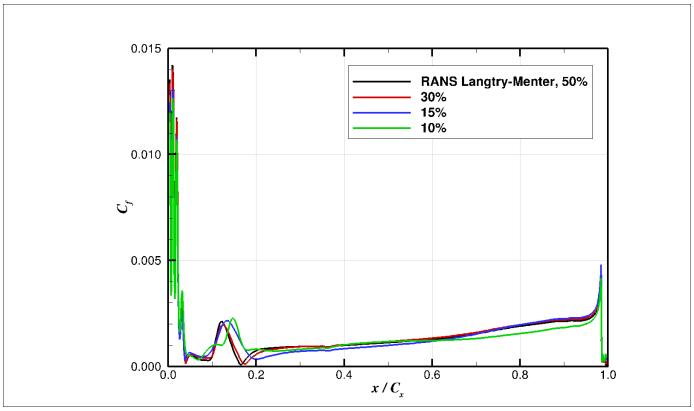

Fig. 36. Skin friction plots for RANS Langtry–Menter takeoff condition at engine-relevant conditions at four spanwise locations: a) suction side and b) pressure side

4.6.3 Efficiency Calculations

Simple turbine-efficiency calculations based only on predicted inlet and exit pressures and temperatures were performed using Eq. 3:

$$\eta_t = \frac{\Delta T}{T_1\left(1.0 - PR^{\frac{1.0-\gamma}{\gamma}}\right)} \tag{3}$$

For the cruise-condition simulation results, a turbine efficiency, η_t, of 59% was calculated. For the takeoff condition, an η_t of 94% was calculated. Although the takeoff condition is an off-design condition, separation was greater for cruise condition at the lower Reynolds-number operation, which is likely why it had a much lower predicted efficiency.

5. Conclusions

A study was performed comparing hybrid RANS/LES and unsteady RANS computations to better understand and predict unsteady separated flow for a linear VSPT cascade blade operating with large incidence angle variation.

Reynolds-number comparisons of RANS results showed some sensitivity of prediction accuracy of blade loadings and wake, as Reynolds number became high but was insensitive to change in the range from 0.4 and 1.0 design $Re_{Cx,2}$. Turbulence intensity comparisons of RANS results showed an insensitivity of prediction of blade loadings to change in turbulence intensity, while prediction of wakes showed some sensitivity to change. However, overall wake-prediction results were only in fair agreement, at best, with the measurements.

For comparisons of results to measurements for blade loading predictions, both RANS Langtry–Menter and hybrid RANS/LES models showed close agreement with the cruise-condition data; however, the RANS Langtry–Menter model compared better with measurements for the takeoff condition.

For comparisons of results with measurements for midspan total pressure loss predictions, all results slightly overpredicted the pitchwise location of the wakes. Overall, the hybrid RANS/LES predictions compared better than the RANS predictions for both the cruise and takeoff conditions.

Comparisons of results for separation predictions were made between the hybrid RANS/LES and RANS Langtry–Menter computations. For the cruise condition, both models predicted shallow separations on the suction side at midspan after approximately $x/C_x = 65\%$. The area of separation predicted near this axial location matches the inflection in the experimental pressure distribution, which suggests that the boundary layer did actually separate there. For the takeoff condition, prediction comparisons revealed significant differences in the presence of separation on the suction side. The RANS Langtry–Menter computations predicted a shallow separation after approximately $x/C_x = 70\%$, while the hybrid RANS/LES computations did not. The area of separation predicted by the RANS Langtry–Menter model near this axial location also matched the inflection in the experimental pressure distribution. This agreement with the data is indicative of the correctness of the RANS Langtry–Menter prediction. For the pressure side, both models predicted a shallow separation bubble across the span close to the leading edge that matched the inflection in the experimental pressure distribution.

Using plots of computed skin friction, comparisons of transition predictions were made between the hybrid RANS/LES and RANS Langtry–Menter computations. Transition predictions were in close agreement between the two models for the

cruise and takeoff conditions. The predicted separation appeared to play a role in transition on the suction side at midspan for the cruise condition for both models. For the takeoff condition, separation induced transition was predicted on the suction side by the RANS Langtry–Menter model but not the hybrid RANS/LES model, and was likely the transition mechanism near the leading edge on the pressure side for both models.

The higher fidelity of the hybrid RANS/LES model did not demonstrate greater accuracy for prediction of separation on the VSPT blade compared with the RANS Langtry–Menter model. However, the hybrid RANS/LES model captured more details of the downstream wake location, as expected. It is possible that the shallowness of the predicted separations presented challenges for hybrid RANS/LES simulations due to their presence mostly within the anisotropic RANS mesh region of the grid, which may have caused the simulation to predict the separation zones with the RANS instead of the LES algorithms of the model. In addition, the use of a periodic single-blade grid and modeling half of the span with a symmetry boundary condition may have had significant effects on the accuracy of the hybrid RANS/LES computations.

Predictions of the VSPT-cascade blade performance at engine-relevant conditions revealed a larger region of separation on the suction side for the cruise condition compared with ambient simulations; however, predictions for the takeoff condition were very similar to results at ambient conditions. Prediction of efficiency is high for the off-design takeoff condition (94%) and low for the cruise condition (59%), which is likely due to the large separation observed at this operating condition.

6. References

1. Spalart PR, Deck S, Shur ML, Squires KD, Strelets MKh, Travin A. A new version of detached-eddy simulation, resistant to ambiguous grid densities. J Theor Comput Fluid Dyn. 2006;20(3):181–195.

2. Basu D, Hamed A, Das K. DES and hybrid RANS/LES models for unsteady separated turbulent flow predictions. Proceedings of the 43rd AIAA Aerospace Sciences Meeting & Exhibit; 2005; Reno, NV. AIAA Paper No.: AIAA-2005-0503.

3. D'Angelo M. Wide speed range turboshaft study. Washington (DC): NASA; 1995. Report No.: NASA/CR–198380.

4. Welch GE. Assessment of aerodynamic challenges of a variable-speed power turbine for large civil tilt-rotor application. Proceedings of the 66th American Helicopter Society International Annual Forum; 2010 May 11–13; Phoenix, AZ. Fairfax (VA): American Helicopter Society International, c2010, p. 345.

5. Flegel-McVetta AB, Giel PW, Welch GE. Aerodynamic measurements of a variable-speed power-turbine blade section in a transonic turbine cascade at low inlet turbulence. Washington (DC): NASA; 2013. Report No.: NASA/TM–2013-218069.

6. Flegel AB, Giel PW, Welch GE. Aerodynamic effects of high turbulence intensity on a variable-speed power-turbine blade with large incidence and Reynolds number variations. Proceedings of the 50th AIAA/ASME/SAE/ASEE Joint Propulsion Conference; 2014 July 28–30; Cleveland, OH. AIAA Paper No. AIAA-2014-3933.

7. Welch GE, McVetta AB, Stevens MA, Giel PW, Ameri, AA, To W, Skoch GJ, Thurman DR. Variable-speed power-turbine research at Glenn Research Center. Proceedings of the 68th American Helicopter Society International Annual Forum; 2012 May 1–3, 2012; Fort Worth, TX. Fairfax (VA): American Helicopter Society International, c2012, p. 2436.

8. Xiao X, McCarter AA, Lakshminarayana B, Pugh E. Tip clearance effects in a turbine rotor: part I – pressure field and loss. ASME J Turbomach. 2000;123(2):296–304.

9. Menter FR, Langtry R, Völker S. Transition modelling for general purpose CFD Codes. J Flow Turb Combust. 2006;77:277–303.

10. Verhoff VG, Camperchioli WP. Lopez I. Transonic turbine blade cascade testing facility. Proceedings of the 17th Aerospace Ground Testing Conference; 1992 July 6–8; Nashville, TN. AIAA Paper No.: AIAA-92-4034.

11. Gie, PW, Sirbaugh JR, Lopez I, Van Fossen GJ. Three dimensional Navier–Stokes analysis and redesign of an imbedded bellmouth nozzle in a turbine cascade inlet section. ASME Journal of Turbomachinery. 1996;118(3):529–535.

12. McVetta AB, Giel PW, Welch GE. Aerodynamic investigation of incidence angle effects in a large scale transonic turbine cascade. Proceedings of the 48th AIAA/ASME/SAE/ASEE Joint Propulsion Conference; 2012 July 30–Aug 1; Atlanta, GA. Paper No.: AIAA-2012-3879.

13. Ford A, Bloxham M, Turner E, Clemens E, Gegg S. Design optimization of incidence-tolerant blading relevant to large civil tilt-rotor power turbine applications. Washington (DC): NASA; 2012. NASA. Report No.: NASA/CR–2012-217016.

14. Booth DT, Flegel AB. 2015, Comparison of computational and experimental results for a transonic variable-speed power-turbine blade operating with low inlet turbulence levels. Proceedings of the 51th AIAA/ASME/SAE/ASEE Joint Propulsion Conference; 2015 July 27–29; Orlando, FL. Paper No.: AIAA-2015-3928.

15. Metacomp Technologies, Inc. CFD++ ver. 16.1.1; 2015 [accessed 2017 Sep 5]. http://www.metacomptech.com/.

16. Metacomp Technologies, Inc. CFD++ and CAA++ user manual ver. 11.1.; 2015 [accessed 2017 Sep 5]. http://www.metacomptech.com/.

17. Shur ML, Spalart PR, Strelets M, Kh, Travin AK. A hybrid RANS-LES approach with delayed-DES and wall-modelled LES capabilities. Int J Heat Fluid Flow. 2008;29(6):1638–1649.

18. Batten P, Goldberg U, Kang E, Chakravarthy S. Smart sub-grid-scale models for LES and hybrid RANS/LES. Proceedings of the 6th AIAA Theoretical Fluid Mechanics Conference; 2011 June 27–30; Honolulu, HI. Paper No.: AIAA-2011-3472.

19. Batten P, Goldberg U, Chakravarthy S. Interfacing statistical turbulence closures with large-eddy simulation. AIAA Journal. 2004;42(3):485–491.

20. Pointwise. Pointwise ver. 17.3; 2015 [accessed 2017 Sep 5]. https::www.pointwise.com /theconnector/2015-February-Special/.

21. White FM. Viscous fluid flow. 3rd ed. New York (NY): McGraw Hill; 2006.

22. Ameri A. Requirements for large eddy simulation computations of variable-speed power turbine flows. Washington (DC): NASA; 2016. Report No.: NASA/CR–2016-218962.

23. Thurman DR, Flegel AB, Giel PW. Inlet turbulence and length scale measurements in a large scale transonic turbine cascade. Proceedings of the 50th AIAA/ASME/SAE/ASEE Joint Propulsion Conference; 2014 July 28–30; Cleveland, OH. Paper No.: AIAA-2014-3934.

24. Wilcox DC. Turbulence modeling for CFD. 3rd ed. Flintridge (CA): DCW Industries, Inc.; 2006.

25. Suchezky M, Cruzen GS. Variable-speed power-turbine for the large civil tilt rotor. Washington (DC): NASA; 2012. Report No.: NASA/CR–2012-217424.

Nomenclature

C_f	skin friction coefficient
Cp_s	static pressure coefficient, $Cp_s = (P - P_2)/(P_{t,1} - P_2)$
Cp_t	total pressure coefficient, $Cp_t = (P_{t,1} - P_t)/(P_{t,1} - P_2)$
C_x	blade axial chord
H	blade span
i	incidence angle (degree), $i = \beta_1$ – inlet metal angle (34.2°)
M	Mach number
P	static pressure
PR	pressure ratio, $PR = P_1/P_2$
P_t	total pressure
Re	Reynolds number, $\mathrm{Re} = \rho U C_x/\mu$
S	blade pitch
T	temperature
Tu	turbulence intensity, $Tu = SQRT(ave\ u'^2_s + ave\ u'^2_z)/U$
u'	fluctuating component of velocity
U	free stream velocity
Δy_{init}	initial distance from the wall to the first wall-adjacent centroid
x	axial coordinate

y	pitchwise coordinate
z	spanwise coordinate
δ	boundary layer thickness
μ	dynamic viscosity
ρ	density
β_1	relative inlet flow angle (degree), $\beta_1 = \tan^{-1}(U_y / U_x)$
γ	ratio of specific heats
η_t	turbine efficiency

Subscripts

1	based on inlet condition
2	based on exit condition
b	baseline
is	isentropic value
s	streamwise component
T	total condition

List of Symbols, Abbreviations, and Acronyms

2-D	two-dimensional
3-D	three-dimensional
ARL	US Army Combat Capabilities Development Command Army Research Laboratory
CFD	computational fluid dynamics
COTS	commercial off-the-shelf
GRC	NASA Glenn Research Center
LES	Large Eddy Simulator
NASA	National Aeronautics and Space Administration
RANS	Reynolds-averaged Navier–Stokes
RANS/LES	Reynolds-averaged Navier–Stokes/Large-Eddy Simulation
RHS	right-hand side
SGS	subgrid scale
VSPT	variable-speed power-turbine

1 (PDF) DEFENSE TECHNICAL INFORMATION CTR DTIC OCA

1 (PDF) CCDC ARL FCDD RLD CL TECH LIB

1 (PDF) CCDC ARL FCDD RLV A D T BOOTH